Spin-Controlled Integrated Near- and Far-Field Optical Launcher

Jiang, Qiao; Bao, Yanjun; Lin, Feng; Zhu, Xing; Zhang, Shuang; Fang, Zheyu

DOI:
10.1002/adfm.201705503

Document Version
Peer reviewed version

Citation for published version (Harvard):
Jiang, Q, Bao, Y, Lin, F, Zhu, X, Zhang, S & Fang, Z 2018, 'Spin-Controlled Integrated Near- and Far-Field Optical Launcher', *Advanced Functional Materials*, vol. 28, no. 8, 1705503. https://doi.org/10.1002/adfm.201705503

Spin-controlled integrated Near- and Far-field Optical Launcher

Yanjun Bao[1†], Qiao Jiang[1,†], Ziwei Li[1,2], Feng Lin[1], Xing Zhu[1], Shuang Zhang[2], and Zheyu Fang[1]

[1]School of Physics, State Key Lab for Mesoscopic Physics, Peking University, Beijing 100871, China

[2] School of Physics and Astronomy, University of Birmingham, Birmingham, B15 2TT, UK.

†These authors contributed equally to this work.

With the evergrowing demand for miniaturization of photonic devices, the integration of different functionalities in a single module is highly desired for the next generation of ultracompact photonic devices. Optical modules for manipulating waves in the near field and far field are both key elements in the construction of nanophotonic devices. Metasurfaces have attracted tremendous interests, because of their flexible ability to manipulate light in either near or far fields_ENREF_3. However, integrating the near- and far-field functionalities into a single module is a great challenge, which hinders the integration and minimization of optical devices. Here, we demonstrate a bifunctional optical launcher by using a single metasurface structure, with which both unidirectional launching of surface plasmon polaritons (SPPs) and focusing of scattered far fields can be simultaneously achieved. Moreover, the SPP propagating direction and the

real/virtual focus of the far-field scattering can be actively controlled by the spin state of the incident light. Our work provides a new platform for the integration and control of different optical components at subwavelength scale, and opens a way to design multifunctional optical devices for the future.

Currently, there is an increasing demand of high-density integration and the miniaturization of photonic elements for the modern information processing. As an emerging branch in nanophotonics, plasmonics has attracted great attention for the ultracompact photonic devices due to its ability to overcome the diffraction limit, and manipulate light at deep subwavelength scale [1-4]. Many photonic modules based on surface plasmon polaritons (SPPs), such as efficient unidirectional optical launcher [5-7], reflectors [8, 9] and demultiplexers [10, 11] have been proposed as the key components for the future plasmonic circuits. On the other hand, optical modules for controlling free space light propagation, such as the metalens [12-15] and optical vortex emitters [16, 17], are also critical components for the photonic circuits. To reduce the size and cost of optical devices, the integration of both the near- and far- field functionalities with a single structure is highly desired.

Metasurface, the two dimensional (2D) analog of metamaterial, is capable of manipulating light in a controllable manner at a subwavelength scale. This is accomplished by the strong optical interaction of space-variant subwavelength artificial structures, with the geometry carefully designed to exhibit desired distributions of amplitude and phase for scattered light[18]. The ultra-thin metasurface provides a novel

route for design of compact optical components. These characteristics make the metasurface a promising candidate for a variety of applications, including the optical spin Hall effect[19-21], anomalous refraction[18, 22-24], metalens[12-15], optical vortex generation[25-27] and optical holography[28-31].

In this work, we propose a method to integrate both the near- and far-field functionalities into a single metasurface design. The metasurface consists of nanoslits perforated in Au film, whose orientations can introduce spatially variant geometric phases for scattering waves in both the near and far fields under circular polarizations. With an additional degree of freedom provided by the positions of the metasurface elements, simultaneous spin-dependent unidirectional near-field launching and the virtual/real far field focusing can be achieved. The bifunctional structure may have potential for the integration and minimization of future optical devices.

Results

Design of the integrated launcher. Figure 1 shows a schematic view of the designed metasurface for an integrated near- and far-field optical launcher. The structure consists of an array of nanoslits perforated in Au film. Upon the illumination of a beam at normal incidence, the nanoslit simultaneously generates SPPs in the near field that propagates along the metallic surface, and scatters the incident light into the far field. Under the circular polarization (CP) incidence, the nanoslit generates locally a geometric phase of $\sigma\theta$ for the surface waves[5, 20], while a geometric phase $2\sigma\theta$ in its cross polarization for the transmitted wave[22, 32], where $\sigma=\pm1$ corresponds to the spin state of right- (RCP)

and left-circular polarization (LCP) for the incident light and θ is the orientation angle of the nanoslit relative to the x axis.

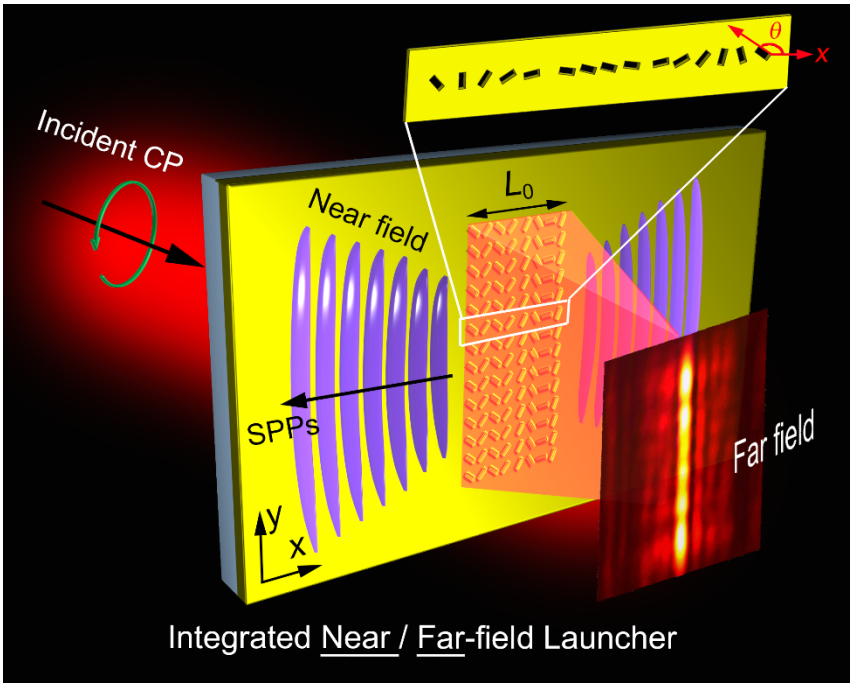

Figure 1| Schematic of the integrated near- and far-field launcher based on metasurface. The metasurface consists of an array of nanoslits with a total length of L_0. Under the illumination of CP light, the nanoslit array excites SPPs in the near field and scatters the incident light into the far field.

By utilizing different geometric phases of the nanoslit in the near and far fields, we are able to integrate both the near- and far-field functionalities into a single structure. In the near field, the SPPs excited by the nanoslit-array at position x_i propagating along the left and right sides ($\pm x$ axis) can be written as

$$E_z(x) \propto \pm \mathrm{e}^{i[\pm k_{spp}(x-x_i)+\sigma\theta]} \qquad (1)$$

where k_{spp} is the SPP wave vector, the positive (+) and negative (-) signs correspond to a SPP propagating to the right and left sides, respectively. Here, by controlling both the position and orientation of each nanoslit, we aim at designing a bifunctional

metasurface that can simultaneously excite unidirectional plasmon propagation and operate as a lens for free space scattering. By requiring that all the SPPs excited by different nanoslits interfere constructively to the right under the LCP (σ=-1) incidence, the following equation can be formulated,

$$-k_{spp}x_i - \theta = const. \tag{2}$$

This condition ensures that the launched SPPs under LCP incidence mainly propagate to the right. For negligible propagation loss of SPPs, the powers to the right and the left are $I_R^{\sigma=-1} \propto \left|\sum_{i=1}^{N} E_z(x_i)\right|^2 = N^2$ and $I_L^{\sigma=-1} \propto \left|\sum_{i=1}^{N} e^{-2i\theta(x_i)}\right|^2$, respectively, where N is the total number of nanoslits along the x direction. The exact power to the left $I_L^{\sigma=-1}$ is dependent on specific orientation angle (i.e. the position) of each nanoslit and is generally much less that to the right $I_R^{\sigma=-1}$ as the constructive interference condition is not satisfied.

Next, to achieve the lens functionality such that the incident LCP light can be focused at the transmitted side, and we then have

$$-2\theta + k\sqrt{x_i^2 + f^2} = const. \tag{3}$$

where k is the wave vector of light in free space and f is the focal distance of the metalens.

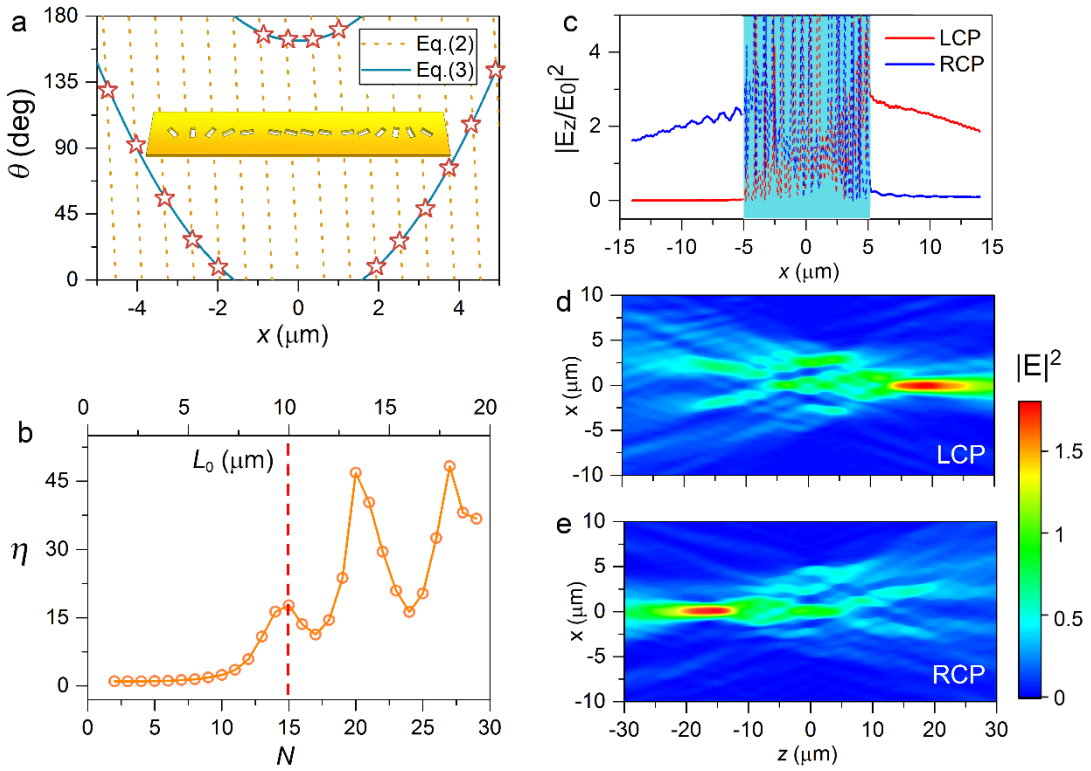

Figure 2| Design of the integrated near- and far-field launcher and the simulation results. (a) Plot of the orientation angle θ of nanoslit as a function of its position x for equations (2) and (3). The inset shows the designed pattern of nanoslits based on the intersection points indicated by star symbols. The length of the metasurface is L_0=10 μm and the number of nanoslits is N=15. **(b)** Extinction ratio as a function of the number of nanoslits N and the total length L_0. The red dashed line indicates the case in **a**. **(c)** Plot of the simulated optical near-field SPP intensities $|E_z|^2$ with LCP (red line) and RCP (blue line) incidences for the structure in **a**. The shaded areas represent the positions of nanoslit metasurface between -5 μm and 5 μm. **(d, e)** Simulated far-field distributions at xz plane with (**d**) LCP and (**e**) RCP incidences.

In order to integrate the optical near- and far-field functionalities in a single device,

equations (2) and (3) need be satisfied simultaneously. Figure 2a shows the relationship between the orientation angle of nanoslit θ and its position x for satisfying both equation (2) (dashed yellow line) and equation (3) (solid blue line) with a focal length f=20 μm at the operating wavelength of 671 nm. The bifunctional metasurface can be realized by choosing the positions of nanoslits at the intersections points (indicated by star symbols), with the distribution shown in the inset of Fig. 2a. With the conventional metasurface design, the positions of constituent plasmonic elements are usually distributed uniformly in space [18, 22]. Here, the extra degree of freedom provided by the positions of the metasurface elements is utilized to achieve the dual functionalities in a single metasurface structure.

Besides achieving the dual functionalities, the designed metasurface is also reconfigurable by the spin of incident light. For the abovementioned metasurface, if the spin state of the incidence is changed to RCP (σ=+1), the powers towards the two opposite directions would be exchanged, i.e. $I_L^{\sigma=+1} = I_R^{\sigma=-1}$ and $I_R^{\sigma=+1} = I_L^{\sigma=-1}$. That is to say, if the SPPs propagate unidirectionally toward one direction under incident light with a certain spin state, the unidirectional launching toward the opposite direction with opposite spin state can be automatically fulfilled. For the far field, equation (3) also guarantees another condition $2\theta - k\sqrt{x_i^2 + f^2} = const.$, which indicates a virtual focus for the RCP incidence (σ=+1). In this case, the polarity of our dual-functional metalens can be changed from positive to negative by switching the polarization of incident light from LCP to RCP.

To estimate the unidirectionality of the launched SPPs in the near field, we define an

extinction ratio $\eta = I_R^{\sigma=-1} / I_L^{\sigma=-1}$, which is the same as $\eta = I_L^{\sigma=+1} / I_R^{\sigma=+1}$. The extinction ratio is a function of the number of nanoslits *N*, as shown in Fig. 2b. With increasing number of nanoslits, the extinction ratio shows a oscillatory feature riding on top of a gradually increasing base. The red dashed line indicates the case in Fig. 2A (*N*=15), with the extinction ratio reaching 17.7.

Numerical and experimental demonstrations of the integrated optical launcher. To confirm the performance of the designed metasurface, we perform finite-difference time-domain (FDTD) simulation of the electric field intensity distributions in the near- and far-field regions (see Method for more details of the numerical calculation). The width and length of each nanoslit is designed as 80 nm and 250 nm, respectively, and the period along the *y* direction is 400 nm. Figure 2c shows the simulated E_z intensity field at a distance 10 nm above the metasurface with *N*=15 under LCP (red line) and RCP (blue line) incidences. The spin-dependent unidirectional launching of SPPs is clearly observed. The simulated extinction ratio is 22 for LCP incidence and 18.2 for RCP incidence, respectively, which is close to the theoretical value of 17.7. The discrepancy between theory and simulation may result from the neglected dissipation of SPPs and the near-field coupling between nanoslits. Figure 2d, e show the far-field intensities at *xz* plane for the two opposite CP lights. For the LCP incidence, a real focal line appears at *z*=20 μm, which agrees with our designed focal length. When the incident polarization is changed to RCP, a virtual focus emerges at the incident side of the metasurface with *z*=-20 μm.

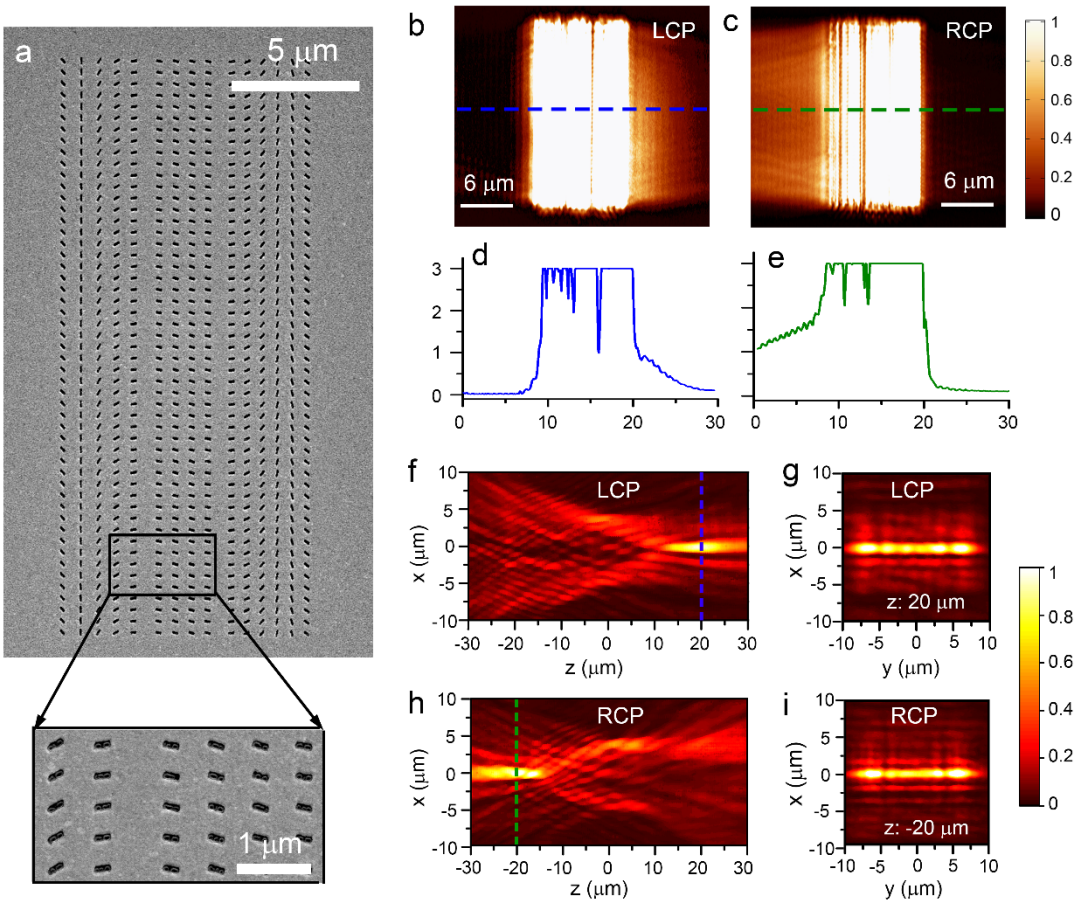

Figure 3| Experimental results of the optical performances in the near and far fields for the 2D metasurface. (a) Scanning electron microscopy (SEM) images of the fabricated 2D metasurface. **(b, c)** Measured optical near-field intensities with (**b**) LCP and (**c**) RCP incidences. **(d, e)** Line-cut of intensities versus *x*-coordinate for the dashed lines in **b**, **c**. **(f, g)** Measured optical far-field intensities at (**f**) *xz* plane and (**g**) real focal *xy* plane (*z*=20 μm) with LCP incidence. **(h, i)** Measured optical far-field intensities at (**h**) *xz* plane and (**i**) virtual focal *xy* plane (*z*=-20 μm) with RCP incidence.

The metasurface is fabricated by evaporating gold film on a glass substrate, followed by focused ion beam (FIB) milling of the nanoslit patterns, as shown in Fig. 3a. To

confirm the dual functionalities, both the near- and far-field optical properties of the metasurface under CP light are measured (See Methods and Supplementary Note 1 for the near-field and far-field measurements). Figure 3b, c show the measured optical near-field intensities by scanning near-field optical microscopy (SNOM), where unidirectional propagation toward each direction with the opposite CP incidence can be observed. From the line-cut of the optical intensities in Fig. 3d, e we can estimate the extinction ratios, which are about 8 and 14 for LCP and RCP incidences, respectively. The measured extinction ratio is smaller than the theoretical calculation, possibly due to the imperfection of the fabrication. Figure 3f-i show the measured far-field intensities at *xz* and *xy* planes for two different incident/transmission polarization combinations: LCP/RCP (Fig. 3f, g) and RCP/LCP (Fig. 3h, i). We can observe a real (virtual) focus at the transmitted (incident) side with z=20 μm (z=-20 μm) for LCP (RCP) incidence. Because the designed metasurface is a 2D periodical structure, the intensities at focal plane (*xy*) show bright focused line along the *y* direction for both CP incidences (Fig. 3g, i).

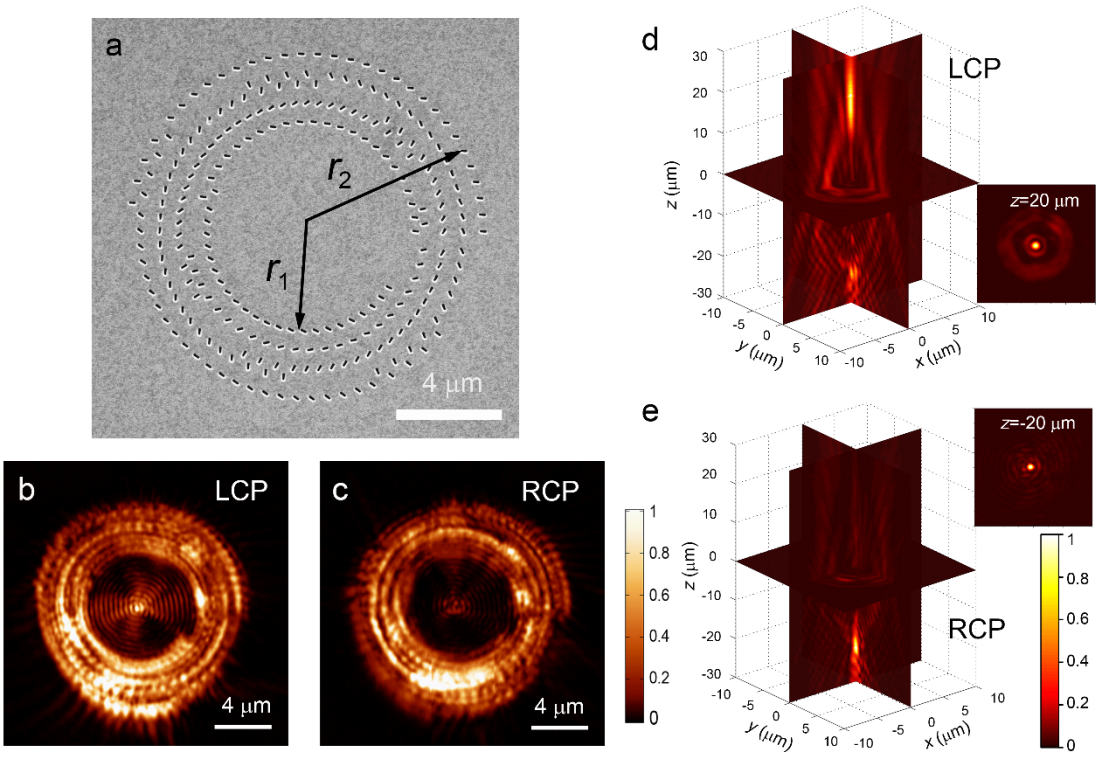

Figure 4| Near- and far-field launching in circular metasurface. (a) SEM figure of the designed circular metasurface with an inner radius of r_1= 3.5 μm and an outer radius of r_2=7 μm. **(b, c)** Measured optical near-field intensity distributions for (**b**) LCP and (**c**) RCP incidences. **(d, e)** Cross-sectional plane views of the measured optical far-field intensity distributions for (**d**) LCP and (**e**) RCP incidences. Inset figures show the intensity distribution at the real and virtual focal (*xy*) planes.

To achieve high-intensity focusing, we modify the metasurface design into a circular configuration, such that both the near field and the scattered far field can be focused into a 2D spot. In the near field, the SPPs generated by each slit propagating toward opposite directions exhibits a π-phase difference, which should be taken into account in the design of the metasurface [20]. The detail of the design is provided in Supplementary Note 2. Figure 4a shows the SEM figure of the circular metasurface, with an inner radius of r_1= 3.5 μm and an outer radius of r_2=7 μm. The measured optical

near-field intensities under LCP incidence is shown in Fig. 4b, where the SPPs propagate radially towards the center and form a high-intensity SPP field at the center, which is consistent with our design. When the incident polarization is changed to RCP (Fig. 4c), the SPP intensity at the center is about 6 times less than that under LCP incidence, since the SPPs primarily propagate outward along the radial directions.

In the far field, a focal-spot point is observed (Fig. 4d, e). The lens is designed with a focal length of 20 μm and a numerical aperture (NA) of 0.33. When the structure is illuminated by a LCP beam, it concentrates light into a real RCP focal point (Fig. 4d). For incident light with an opposite spin of RCP, a virtual LCP focal point emerges at the incident side of the lens (Fig. 4e). The focal spot size is measured to be about 960 nm at full width at half maximum, which is close to the diffraction-limited spot size (λ/2NA).

Discussion

It is important that multiple functionalities integrated into a single device do not interfere with each other. Here we compare the optical performance of our designed bifunctional structure with the one that has single functionality (far-field focusing or unidirectional launching of SPPs only). In the design of the far-field focusing, because constructive-interference condition is satisfied for both the single-functional and our bi-functional structures, the focal intensities should be the same if they contain the same number of metasurface elements with the same geometry. In the near field, although the SPPs constructively interfere along one direction and cannot be completely canceled

along the opposite direction, the extinction ratio of our structure can be at least comparable to that with a single functionality [6, 33, 34], due to the additional degree of freedom provided by the positions of the metasurface elements. Thus, our designed metasurface can not only integrate both functionalities in a single structure, but also maintain good optical performances.

In summary, we proposed and experimentally demonstrated an integrated near- and far-field launcher with designed metasurface. By flipping the spin state of the incident light, we show that unidirectional launching of SPPs toward either direction of the periodical metasurface can be realized and meanwhile the polarity of the metalens can be switched between negative and positive. We further designed a metasurface for focusing both near field and far field wave propagation into focal spots. Although each functionality demonstrated here has been individually realized previously, the integration of them in a single structure is highly desired for the device minimization. Our work may provide new ideas for further design of multifunctional integrated optical devices.

Methods

Numerical calculations. The optical near and far fields are numerically calculated by FDTD method. The virtual fields, which are contributed by the transmitted light and formed at the incident side of the metasurface if they were projected backward, cannot be directly obtained from the simulation. To calculate the virtual fields, we first record the field distribution of a *xy* plane located at the transmitted side of the metasurface

(z>0). An near- to far-field projection is employed to calculate the angular distribution of the far field $E(k_x)$, where k_x is the x component of the wave vector of light. The fields with the circular polarization opposite to that of the incident wave are extracted as $E'(k_x)$. The total field can be obtained by summing all the plane waves multiplied by a phase factor as $E(x,z)=\sum_{k_x} E'(k_x)e^{i(k_x x+k_z z)}$, where $k^2=k_x^2+k_z^2$. The far-field distribution at both real (z>0) and virtual regions (z<0) can be calculated directly.

Sample fabrication and experimental measurements. The samples were fabricated by evaporating 120-nm-thick gold film on a glass substrate and a following focused ion beam (FIB) milling of the nanoslit patterns. For optical measurement, the incident CP light with wavelength of 671 nm was generated by a quarter-wave plate (QWP) and a polarizer. The sample was mounted on a three-dimensional stage, which is able to accurately control the movement of the sample. The SPPs were measured by a SNOM probe, which can collect the SPP signals and couple it into propagating modes in the optical fiber. The transmitted light through the metasurface in the far field was collected with an objective (40×/0.75) and imaged on a CMOS camera after passing through another pair of QWP and polarizer. A schematic of the optical setup is shown in Supplementary Fig. 1.

Acknowledgements

This work is supported by the National Key Research and Development Program of China (grant no. 2017YFA0206000), National Basic Research Program of China (grant no. 2015CB932403, 2017YFA0205700), National Science Foundation of China (grant

nos. 61422501, 11674012, 11374023, and 61521004), Beijing Natural Science Foundation (grant no. L140007), and Foundation for the Author of National Excellent Doctoral Dissertation of PR China (grant no. 201420), National Program for Support of Top-notch Young Professionals.

Author contributions

Y. B. and Z. F. conceived the concept. Y. B. conducted the numerical simulations. Q. J. performed the optical experiments. Z. F. supervised the project. All authors discussed the results and commented on the paper.

Additional information

Supplementary information is available in the online version of the paper. Reprints and permission information is available online at http://www.nature.com/reprints. Correspondence and requests for materials should be addressed to Z. F.

Competing financial interests

The authors declare no competing financial interests.

References

1. Zayats, A. V., Smolyaninov, I. I.& Maradudin, A. A. Nano-optics of surface plasmon polaritons. *Phys. Rep.* **408**, 131-314 (2005).
2. Maier, S. A. *Plasmonics: Fundamentals and Applications*. Springer: New York, 2007.
3. Ozbay, E. Plasmonics: merging photonics and electronics at nanoscale dimensions. *Science* **311**,

189-193 (2006).
4. Barnes, W. L., Dereux, A.& Ebbesen, T. W. Surface plasmon subwavelength optics. *Nature* **424**, 824-830 (2003).
5. Lin, J., et al. Polarization-controlled tunable directional coupling of surface plasmon polaritons. *Science* **340**, 331-334 (2013).
6. López-Tejeira, F., et al. Efficient unidirectional nanoslit couplers for surface plasmons. *Nat. Phys.* **3**, 324-328 (2007).
7. Bao, Y., Zu, S., Zhang, Y.& Fang, Z. Active Control of Graphene-Based Unidirectional Surface Plasmon Launcher. *ACS Photonics* **2**, 1135-1140 (2015).
8. Hosseini, A.& Massoud, Y. A low-loss metal-insulator-metal plasmonic bragg reflector. *Opt. Express* **14**, 11318-11323 (2006).
9. Liu, J. Q., et al. A wide bandgap plasmonic Bragg reflector. *Opt. Express* **16**, 4888-4894 (2008).
10. Li, L., Li, T., Wang, S. M., Zhu, S. N.& Zhang, X. Broad Band Focusing and Demultiplexing of In-Plane Propagating Surface Plasmons. *Nano Lett.* **11**, 4357-4361 (2011).
11. Zhao, C. L.& Zhang, J. S. Plasmonic Demultiplexer and Guiding. *Acs Nano* **4**, 6433-6438 (2010).
12. Khorasaninejad, M., et al. Metalenses at visible wavelengths: Diffraction-limited focusing and subwavelength resolution imaging. *Science* **352**, 1190-1194 (2016).
13. Wang, Q., et al. Optically reconfigurable metasurfaces and photonic devices based on phase change materials. *Nat. Photonics* **10**, 60-65 (2016).
14. Chen, X., et al. Longitudinal Multifoci Metalens for Circularly Polarized Light. *Adv. Opt. Mater.* **3**, 1201-1206 (2015).
15. Ni, X., Ishii, S., Kildishev, A. V.& Shalaev, V. M. Ultra-thin, planar, Babinet-inverted plasmonic metalenses. *Light Sci. Appl.* **2**, e72 (2013).
16. Cai, X. L., et al. Integrated Compact Optical Vortex Beam Emitters. *Science* **338**, 363-366 (2012).
17. Yang, Y., et al. Dielectric meta-reflectarray for broadband linear polarization conversion and optical vortex generation. *Nano Lett.* **14**, 1394-1399 (2014).
18. Yu, N., et al. Light propagation with phase discontinuities: generalized laws of reflection and refraction. *Science* **334**, 333-337 (2011).
19. Yin, X. B., Ye, Z. L., Rho, J., Wang, Y.& Zhang, X. Photonic Spin Hall Effect at Metasurfaces. *Science* **339**, 1405-1407 (2013).
20. Bao, Y., et al. Revealing the spin optics in conic-shaped metasurfaces. *Phys. Rev. B* **95**, 081406 (2017).
21. Xiao, S., Zhong, F., Liu, H., Zhu, S.& Li, J. Flexible coherent control of plasmonic spin-Hall effect. *Nat. Commun.* **6**, 8360 (2015).
22. Huang, L., et al. Dispersionless phase discontinuities for controlling light propagation. *Nano Lett.* **12**, 5750-5755 (2012).
23. Sun, S., et al. High-efficiency broadband anomalous reflection by gradient meta-surfaces. *Nano Lett.* **12**, 6223-6229 (2012).
24. Lin, D., Fan, P., Hasman, E.& Brongersma, M. L. Dielectric gradient metasurface optical elements. *Science* **345**, 298-302 (2014).
25. Pu, M., et al. Catenary optics for achromatic generation of perfect optical angular momentum. *Science Advances* **1**, e1500396 (2015).
26. Maguid, E., et al. Photonic spin-controlled multifunctional shared-aperture antenna array. *Science* **352**, 1202-1206 (2016).

27. Yu, N. F.& Capasso, F. Flat optics with designer metasurfaces. *Nat. Mater.* **13**, 139-150 (2014).
28. Khorasaninejad, M., Ambrosio, A., Kanhaiya, P.& Capasso, F. Broadband and chiral binary dielectric meta-holograms. *Science Advances* **2**, e1501258 (2016).
29. Wen, D. D., et al. Helicity multiplexed broadband metasurface holograms. *Nat. Commun.* **6**, 8241 (2015).
30. Arbabi, A., Horie, Y., Bagheri, M.& Faraon, A. Dielectric metasurfaces for complete control of phase and polarization with subwavelength spatial resolution and high transmission. *Nat. Nanotechnol.* **10**, 937-943 (2015).
31. Zheng, G., et al. Metasurface holograms reaching 80% efficiency. *Nat. Nanotechnol.* **10**, 308-312 (2015).
32. Chen, X., et al. Dual-polarity plasmonic metalens for visible light. *Nat. Commun.* **3**, 1198 (2012).
33. Rodriguez-Fortuno, F. J., et al. Near-field interference for the unidirectional excitation of electromagnetic guided modes. *Science* **340**, 328-330 (2013).
34. Liu, Y., et al. Compact magnetic antennas for directional excitation of surface plasmons. *Nano Lett.* **12**, 4853-4858 (2012).